CORA Cork Open Research Archive
Cartlann Taighde Oscailte Chorcaí

Title	Synthesis of millimeter-sized Mo x W (1– x) S 2 y Se 2(1– y) monolayer alloys with adjustable optical and electrical properties and their magnetic doping
Authors	Li, You;Wang, Yiwen;Hussain, Sabir;Xie, Liming;Qi, Junjie
Publication date	2023-11-21
Original Citation	Li, Y., Wang, Y., Hussain, S., Xie, L. and Qi, J. (2023) 'Synthesis of millimeter-sized Mo x W (1– x) S 2 y Se 2(1– y) monolayer alloys with adjustable optical and electrical properties and their magnetic doping', Journal of Materials Chemistry C, 11(48), pp. 16912–16921. Available at: https://doi.org/10.1039/D3TC03332E.
Type of publication	Article (peer-reviewed)
Link to publisher's version	10.1039/D3TC03332E
Rights	© The Royal Society of Chemistry 2023
Download date	2026-11-02 19:49:04
Item downloaded from	https://hdl.handle.net/10468/15359

UCC
University College Cork, Ireland
Coláiste na hOllscoile Corcaigh

Journal of Materials Chemistry C

ROYAL SOCIETY OF CHEMISTRY

REVIEW

View Article Online
View Journal | View Issue

Published on 21 November 2023. Downloaded by University College Cork on 1/11/2024 3:55:58 PM.

Check for updates

Cite this: J. Mater. Chem. C, 2023, 11, 16912

Synthesis of millimeter-sized $Mo_xW_{(1-x)}S_{2y}Se_{2(1-y)}$ monolayer alloys with adjustable optical and electrical properties and their magnetic doping†

You Li,[a] Yiwen Wang,[a] Sabir Hussain,[b] Liming Xie[b] and Junjie Qi*[a]

Received 13th September 2023,
Accepted 20th November 2023

DOI: 10.1039/d3tc03332e

rsc.li/materials-c

Alloying has emerged as an effective approach for elec/optoelectronics applications by modulating the bandgap engineering of two-dimensional (2D) transition metal dichalcogenides (TMDs). Based on our earlier liquid phase edge epitaxy (LPEE) method, we have grown millimeter-sized quaternary $Mo_xW_{(1-x)}S_{2y}Se_{2(1-y)}$ monolayer films and $Mo_xW_{(1-x)}S_{2y}Se_{2(1-y)}$ monolayers with different morphologies by controlling the growth temperature and time. The homogeneity and good crystallinity of as-grown alloys are demonstrated by energy-dispersive spectroscopy (EDS), elemental mapping, Raman mapping, and high-resolution transmission electron microscopy (HRTEM). Atomic-resolution scanning transmission electron microscopy (STEM) strongly demonstrates the uniform distribution of Mo, W, S, and Se. Furthermore, alloy-based field-effect transistors (FETs) displaying bipolar conduction behavior with a weak p-branch and conduction behavior show component-dependent properties. In addition, this strategy has been broadened to prepare M-doped $Mo_xW_{(1-x)}S_{2y}Se_{2(1-y)}$ monolayers (M: Fe, Co, and Ni) for the first time, where magnetic hysteresis (M–H) measurements indicated room temperature ferromagnetism of $Mo_xW_{(1-x)}S_{2y}Se_{2(1-y)}$. Therefore, the synthesized pristine and M-doped alloys have greatly enriched the family of 2D materials and are prospective candidates for applications in future industrial device applications.

Introduction

Two-dimensional (2D) transition metal dichalcogenides (TMDs) have promising applications in elec/optoelectronics, catalysis, and energy owing to their unique crystal structures and novel physical and chemical properties.[1–10] For instance, the monolayers of MX_2 (M: Mo, W and X: S, Se) have advantages including large exciton binding energy,[11] direct bandgap,[12] robust valley polarization,[13] strong light–matter coupling,[14] and high optical absorption coefficient,[15] which makes them a hot spot for device applications.[16–19] However, binary TMDC monolayers still have limitations because of their inherent bandgap, where researchers can significantly broaden their application fields through bandgap engineering. The band gaps of 2D TMDs can be adjusted by alloying, strain applications, doping, and functionalization to improve the performance of TMD-based monolayer devices.[20–23] Among them, alloying is an effective method to synthesize TMDCs with tunable bandgaps by adjusting the composition. So far, the research has mainly focused on $MoS_{2(1-x)}Se_{2x}$,[24] $WS_{2(1-x)}Se_{2x}$,[25–27] $Mo_{1-x}W_xS_2$ and other ternary alloys.[28–32] However, the addition of a fourth element can provide greater flexibility for changing the electronic properties. Fewer studies have also been conducted on quaternary TMDC monolayer alloys and the size of the prepared alloys is small, which is difficult to meet the rapid development of device technology. It has been emphasized that quaternary monolayer $Mo_xW_{(1-x)}S_{2y}Se_{2(1-y)}$ alloys with MX_2 stoichiometry proved to be stable due to the similar atomic structure and properties of selenides and sulfides. Since the individual MX_2 compositions have a wide band gap range (*e.g.*, $MoSe_2$-1.55 eV, WSe_2-1.65 eV, MoS_2-1.85 eV, and WS_2-1.95 eV), their optical properties are highly tunable.[33]

To obtain high-quality monolayer TMDC alloys, various approaches have been developed including physical vapor deposition (PVD),[36] molecular beam epitaxy (MBE),[35] mechanical exfoliation (ME),[34] chemical vapor deposition (CVD),[37–40] *etc.* But, phase separation is usually inevitable in the synthesis of alloys using conventional CVD, as the inhomogeneous distribution of different vaporization precursors can lead to

[a] School of Materials Science and Engineering, University of Science and Technology Beijing, Beijing 100083, P. R. China. E-mail: junjieqi@ustb.edu.cn
[b] CAS Key Laboratory of Standardization and Measurement for Nanotechnology, National Center for Nanoscience and Technology, Beijing 100190, China

† Electronic supplementary information (ESI) available. See DOI: https://doi.org/10.1039/d3tc03332e

This journal is © The Royal Society of Chemistry 2023

Published on 21 November 2023. Downloaded by University College Cork on 1/11/2024 3:55:58 PM.

undesired reactions in the furnace.[41–43] At the same time, it is almost impossible to achieve high-quality TMD alloys incorporating more than two anionic elements by a conventional CVD method due to the significantly varying evaporation temperatures, saturation vapor pressures, and reaction energies of diverse precursors.[44] Thus, the controlled synthesis of monolayer films of quaternary alloys with large size and high crystal quality remains a great challenge. In addition, dilute magnetic semiconductors (DMSs) with both semiconductivity and magnetism have been widely investigated by doping magnetic transition elements such as Fe, Co, and Ni.[45–49] The presence of magnetic anisotropy in two-dimensional crystals affects the excitation of low-energy spin waves, which suppresses the thermal uplift and stabilizes the alignment of spins in a particular direction, ultimately achieving magnetism. Many other novel physical phenomena have been observed in dilute magnetic semiconductors, such as anisotropic magneto-resistance (AMR), giant planar hall effect (GPHE), *etc.*, which make them promising for spintronics applications. Obviously, the pursuit of the controlled synthesis of multiple transition metal chalcogenides and magnetic transition metal-doped monolayer TMD functional materials is the basis for the realization of these materials.

In previous work, we developed a more universal self-limiting growth method for high-quality 2D monolayers: liquid-phase edge epitaxy (LPEE).[50] In this LPEE method, MoS_2 and WSe_2 are used as the precursors, and CsCl with high surface tension is selected as the flux. According to the previous achievement of our group, the growth of monolayers is preferable for the solvent with higher surface tension.[50] The solution contacts the 2D grains only at the grain edges, which limits the epitaxy along the in-plane direction, thus achieving monolayer growth of quaternary monolayer $Mo_{1-x}W_xS_{2y}Se_{2(1-y)}$ alloys. STEM examined the quality of the prepared alloys, indicating high-quality single-crystal domains. The fabricated alloy-based FETs displaying bipolar conduction behavior with a weak p-branch and conduction behavior show component-dependent properties. So far, the study of magnetically M-doped $Mo_xW_{(1-x)}$ $S_{2y}Se_{2(1-y)}$ monolayer alloys has not been reported yet. In addition, we have successfully broadened this strategy by magnetically M-doping into quaternary alloys. The prepared M-doped $Mo_xW_{(1-x)}$ $S_{2y}Se_{2(1-y)}$ has demonstrated ferromagnetic response at room temperature. The synthesized pristine and M-doped alloys have greatly enriched the family of 2D materials and are prospective candidates for future industrial applications.

Results and discussion

A typical procedure for the preparation of monolayer $Mo_xW_{(1-x)}$ $S_{2y}Se_{2(1-y)}$ alloys by the LPEE method is shown in Fig. 1(a). CsCl

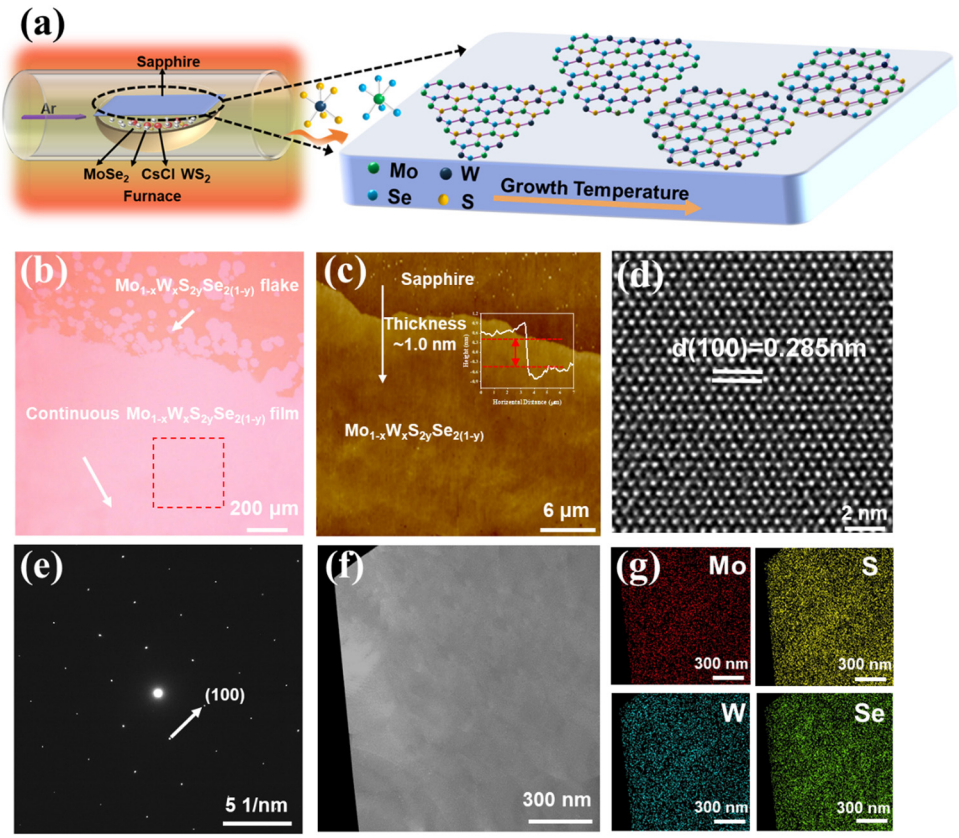


Fig. 1 LPEE of large-area $Mo_xW_{(1-x)}$ $S_{2y}Se_{2(1-y)}$. (a) Illustration of the monolayer alloy's growth. (b)–(g) Optical image, AFM image (with the inset of the height profile), HRTEM image, SAED image, STEM image, and EDS mapping images of the as-grown $Mo_xW_{(1-x)}$ $S_{2y}Se_{2(1-y)}$ monolayers at 900 °C, respectively.

Published on 21 November 2023. Downloaded by University College Cork on 1/11/2024 3:55:58 PM.

was laid flat on the MX_2 precursor and then the sapphire substrate was inverted on a quartz boat and placed in the center of the heating furnace. Prior to heating, Ar stream was passed through the system to ensure an oxygen-free environment for the growth of $Mo_xW_{(1-x)}$ $S_{2y}Se_{2(1-y)}$ alloys, and the tube furnace was then programmed to heat up to the specified temperature (825 °C–900 °C), and maintain the temperature for 0–120 min. Compared with the previously reported conventional vapor deposition growth methods, the LPEE method exhibits the following advantages in the synthesis of large-size homogeneous monolayer $Mo_xW_{(1-x)}$ $S_{2y}Se_{2(1-y)}$ alloys: (1) the face-to-face source–substrate structure ensures a sufficient, uniform, and stable supply of precursors, which is essential for the development of crystalline domains with large dimensions on the substrate surface. (2) The LPEE method limits the growth of $Mo_xW_{(1-x)}$ $S_{2y}Se_{2(1-y)}$ alloys in the vertical direction due to the presence of droplets so that the materials can only grow in the horizontal direction and eventually form a monolayer, which makes the thickness controllable. Meanwhile, the CVD growth process will appear in the sample when the thickness varies. The detailed mechanism for the preparation of monolayer alloys by the LPEE method is discussed in Fig. S1 (ESI†). (3) The process of the LPEE method is safer since no chemical reactions are involved, the reaction process will not produce toxic by-products, the product purity is high, the impurity is low, and the quality of the crystals is high. (4) Doping with other elements (Fe-, Co-, and Ni) by the LPEE method is easy.

Fig. 1(b) illustrates an optical micrograph of the region near the edges of $Mo_xW_{(1-x)}$ $S_{2y}Se_{2(1-y)}$ alloy films (900 °C/120 min). As can be seen from the image, the film is shaped by many regular hexagonal $Mo_xW_{(1-x)}$ $S_{2y}Se_{2(1-y)}$ alloy domains bound together. On the upper side, individual (regular hexagonal) crystalline domains can be seen. On the lower side, the film becomes continuous with a lateral dimension of 1.4 mm, much larger than that previously reported in the literature.[51,52] For more clarity, we obtained a large-size optical microscopy (OM) image of $Mo_xW_{(1-x)}$ $S_{2y}Se_{2(1-y)}$ alloy films at a high magnification (Fig. S2(a and c), ESI†), without sharp interfaces. The surface morphology of $Mo_xW_{(1-x)}$ $S_{2y}Se_{2(1-y)}$ monolayer films was characterized using an atomic force microscope (AFM). Fig. 1(c) and Fig. S2 (b, d) (ESI†) show the typical AFM images and thickness profile of $Mo_xW_{(1-x)}$ $S_{2y}Se_{2(1-y)}$ alloys, where the homogeneous color contrast indicates a flat and smooth surface. Cross-sectional analysis displays the thickness of the as-grown alloy to be about 1 nm, thus confirming a monolayer. The HRTEM image shows that alloy monolayers maintain a regular hexagonal lattice structure with a lattice spacing of 0.285 nm along the (100) direction (Fig. 1(d)). A set of hexagonally arranged diffraction points of SAED indicate the good crystallinity of as-grown alloys (Fig. 1(f)). Furthermore, the EDS elemental mappings identically display the homogeneous

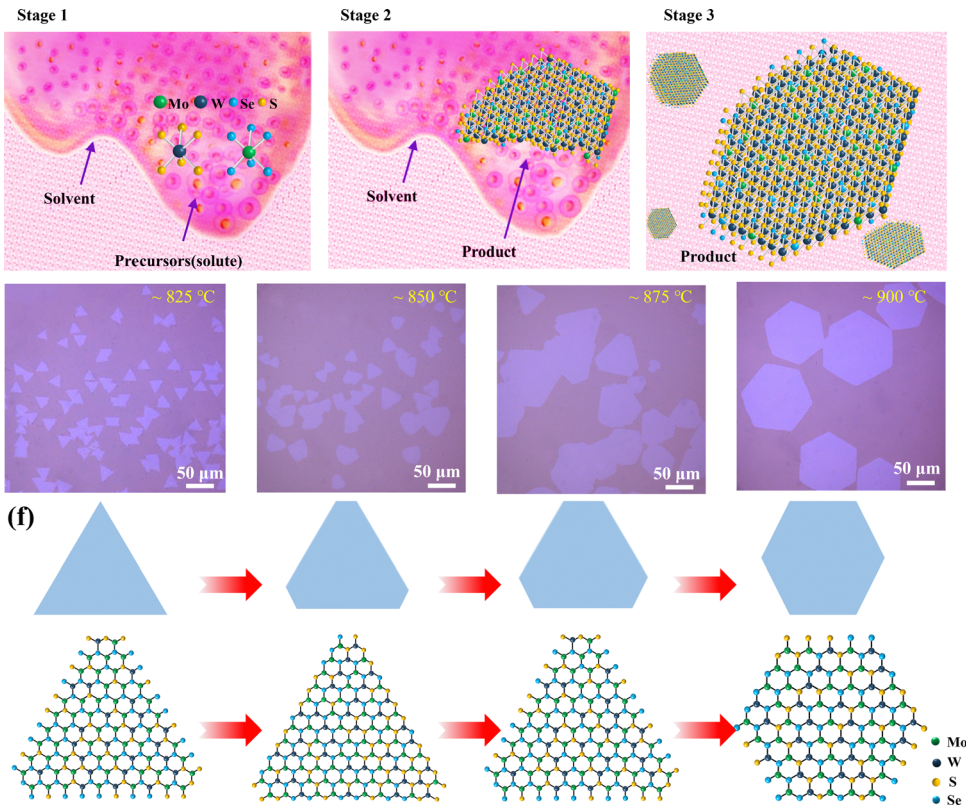


Fig. 2 Growth of $Mo_xW_{(1-x)}$ $S_{2y}Se_{2(1-y)}$ monolayers by LPEE. (a) Schematic of LPEE for the growth of $Mo_xW_{(1-x)}$ $S_{2y}Se_{2(1-y)}$ monolayers. (b)–(e) Optical images of $Mo_xW_{(1-x)}$ $S_{2y}Se_{2(1-y)}$ monolayers obtained at different growth temperatures. (f) Schematic diagrams and proposed structures of different morphologies at different temperatures.

 This journal is © The Royal Society of Chemistry 2023

Published on 21 November 2023. Downloaded by University College Cork on 1/11/2024 3:55:58 PM.

distribution of Mo, W, S, and Se elements, proving that the alloy composition was uniformly distributed and free of agglomerated particles and nanocrystals (Fig. 1(f and g)).

Fig. 2(a) illustrates that the quaternary monolayer alloys were obtained by using the molten solution on substrates. The growth process of our LPEE method includes: (a) solute atoms from the solid-phase materials are transported in the solution by diffusion and convection (stage 1); (b) solute atoms diffuse to the surface and the solute is precipitated at the interface between the solution and the substrate (stage 2); (c) finally, most of the solvent is volatilized and salts are left on substrates after growth (stage 3). Furthermore, the growth temperature and time have been found to be key factors in determining the size and morphology of $Mo_xW_{(1-x)}$ $S_{2y}Se_{2(1-y)}$. We set various growth temperatures while ensuring a consistent growth time (60 min), and different morphologies of as-grown alloys could be observed (Fig. 2(b–e)). The triangular morphology with straight edges is obtained at a low temperature of 825 °C. As the temperature increases, the gradual increase in the size of monolayer alloys and morphology change to irregular triangles. Hexagonal shapes with straight edges are obtained at a high temperature of 900 °C. This progressive morphological change may be related to the kinetic growth mechanism, where the non-ideal transition metal/chalcogenide atomic ratio induces a non-equilibrium growth state at the growth interface.[8,53] Fig. S3 (ESI†) shows the OM diagrams of the as-grown alloy at 900 °C for different growth times (0–120 min). It can be seen that the sample morphologies are all regular hexagonal. With the increase in growth time, the size of alloys gradually becomes larger. The average size of the as-grown alloys increases almost linearly from 30 μm to 120 μm.

We performed photoluminescence (PL) tests on the alloys prepared at different temperatures (Fig. 3(a)), and the spectra all exhibited a single emission peak, without observing any defect peaks or structural disorder peaks associated with low-energy emission, indicating that the components in the as-grown alloys are uniformly mixed without phase segregation and crystal quality are generally excellent. As the growth temperature increases, the PL peak shifts to a shorter wavelength (from 783 nm to 684 nm), indicating an improvement in the concentration of W and S in the alloy (WS_2 has a larger forbidden band than $MoSe_2$). Meanwhile, we have characterized the structure of monolayer $Mo_xW_{(1-x)}$ $S_{2y}Se_{2(1-y)}$ alloys prepared at different temperatures by Raman spectroscopy measurements (Fig. 3(b)). The Raman peak corresponding to E_{2g}(S–W) − LA(S–W) + E_{2g}(Se–W) − LA(Se–W) caused mainly by W–S–Se vibrations is observed at 162.53 cm^{-1}, where LA represents the longitudinal acoustic mode. The peak observed at 265.65 cm^{-1} is attributed to the A_{1g} modes of W–Se and Mo–Se bond vibrations. The peak observed at 330.22 cm^{-1} belongs to the Mo–W–S–Se-bond vibrational modes.[51] The E_{2g} peaks of sulfide exhibit bimodal behavior at 353.11 cm^{-1} and 381.54 cm^{-1}, attributed to E_{2g} (Mo–S) and E_{2g} (W–S), respectively. Finally, the A_{1g} peak attributed to the combined W–S and Mo–S vibrations is observed at 412.81 cm^{-1}. In addition, it can be seen from the graph that the peak position does not shift greatly with the increasing temperature, but the peak intensity gradually increases, which indicates that the proportion of heavier W atoms entering the internal lattice of the alloy increases at higher temperatures.

To investigate the continuity and homogeneity of the as-grown monolayer alloy films, we selected the region marked by

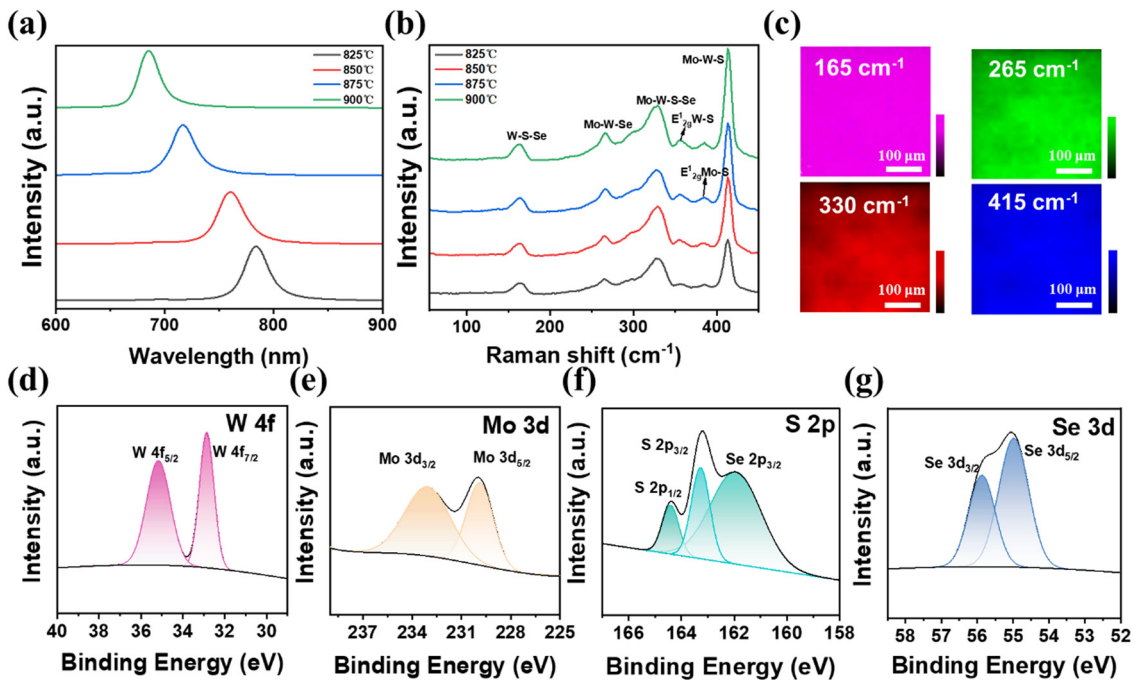


Fig. 3 Characterization of $Mo_xW_{(1-x)}$ $S_{2y}Se_{2(1-y)}$ monolayers at different temperatures. (a) and (b) Raman spectra and PL spectra, respectively. (c) Raman mapping images of the selected area in Fig. 1b. (d)–(g) XPS scans of W 4f, Mo 3d, S 2p, and Se 3d, respectively at 900 °C.

Published on 21 November 2023. Downloaded by University College Cork on 1/11/2024 3:55:58 PM.

the red rectangle in the panel of Fig. 1(b) for Raman mapping images (Fig. 3(c)). The thin film shows a uniform distribution of the four phases with a few dark regions corresponding to anion vacancies. For experimental accuracy, additionally, we randomly selected 50 positions on the monolayer $Mo_xW_{(1-x)}S_{2y}Se_{2(1-y)}$ alloy film for Raman measurements (Fig. S4, ESI†)), and all Raman spectra exhibit the same peak pattern and intensity uniformity, again demonstrating the homogeneity of the monolayer alloy. The chemical composition and structure of the monolayer $Mo_xW_{(1-x)}$ $S_{2y}Se_{2(1-y)}$ alloys were observed using X-ray photoelectron spectroscopy (XPS) (Fig. 3(d–g). The XPS results clearly reveal the coexistence of W, Mo, S, and Se atoms in the synthesized alloys (Fig. S5, ESI†). The element ratio of quaternary alloys was calculated by XPS spectra (Table S1, ESI†).

The atomic structures of the as-grown monolayer alloys were studied by STEM. We can visualize the distribution of Se, W, S and Mo atoms in the monolayer $Mo_xW_{(1-x)}$ $S_{2y}Se_{2(1-y)}$ alloys by atomic imaging with high-angle annular dark-field scanning transmission electron microscopy (HAADF-STEM), further demonstrating the good crystallinity of the as-grown alloys (Fig. 4(a)). The intensity distribution along the marked red solid box in Fig. 4(b) highlights the occupancies of Mo, W, S, and Se sites (Fig. 4(c)). Based on the intensity differences between the atoms in the HAADF-STEM images, we performed the statistical analysis in the STEM images, dividing the atoms in the image into metal (M) sites and sulfur (X_2) sites (Fig. 4(d and e)). The intensity histograms of all metal sites show two peaks, in the descending order of intensity, for the Mo site and the W site. The intensity histograms of all X_2 sites show three peaks, with the SS site, SSe site, and SeSe site in the descending order of intensity. By recognizing peaks in the HAADF intensity, the atom type can be determined, resulting in an atomic labeling image as shown in Fig. S6 (ESI†). From the images, the elements in each sample are uniformly distributed, demonstrating the good mixing of the elements at 825 °C.

To evaluate the effect of the electronic structure changes of as-grown alloys, back-gated FET devices were prepared with Cr/Au (10/60 nm) as source–drain electrodes deposited on SiO_2/Si. As shown in Fig. 5(a), the pure MoS_2 FET displays an insulating nature at a large negative gate bias and is turned on at V_{gs} = −70 V, exhibiting strong n-type conduction with a high I_{on}/I_{off} ratio of about 10^7 for V_{gs} sweep from −80 to +80 V. The output (I_{ds}–V_{ds}) curves were measured at different V_{gs} (Fig. 5(b)), indicating a typical ohmic contact between the electrodes and the sample channel with good contact, in agreement with previous studies. For the as-grown alloys shown in Fig. 5(c–f), it shows a weak p-branch bipolar characteristic with a significantly lower switching ratio. The output curves show good linearity (Fig. S7(a–d), ESI†). It is noteworthy that the I_{on}/I_{off} ratio of the alloy-based FETs gradually decreases with the increasing growth temperature, which may be may be since WSe_2 is a p-type semiconductor and the increase in temperature

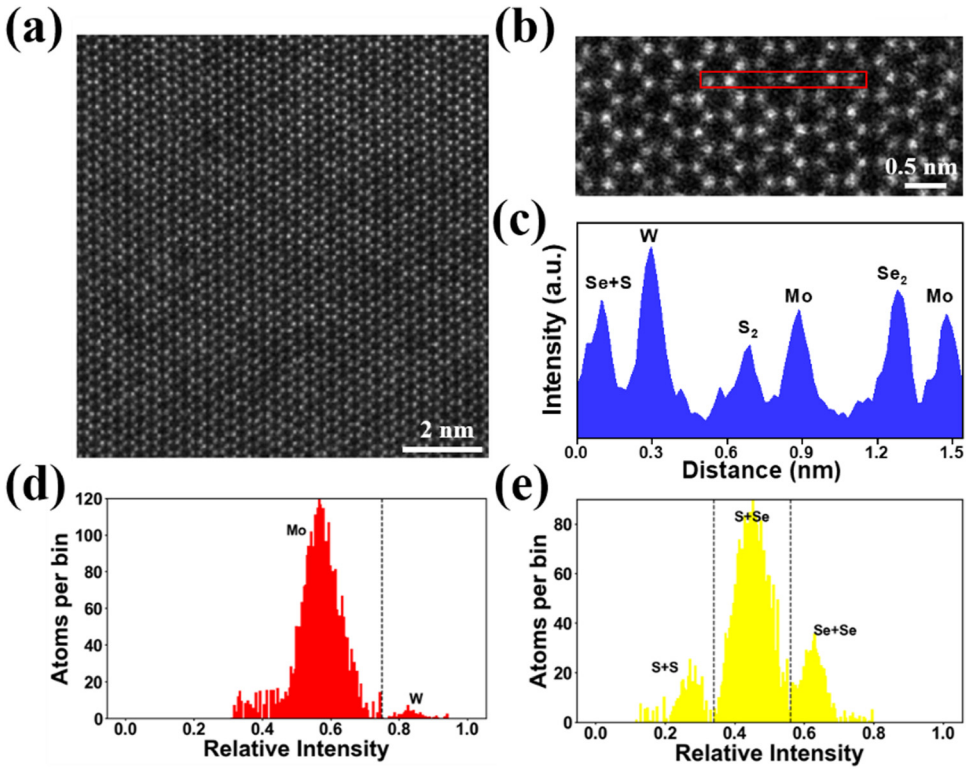


Fig. 4 Atomic characterization of $Mo_xW_{(1-x)}$ $S_{2y}Se_{2(1-y)}$ monolayers at 825 °C. (a) and (b) HAADF-STEM images of the as-grown $Mo_xW_{(1-x)}$ $S_{2y}Se_{2(1-y)}$ monolayer. (c) Intensity profile along the marked red solid box in (b). (d) and (e) The corresponding statistical HAADF intensity histograms of the M and X_2 sites, respectively.

 This journal is © The Royal Society of Chemistry 2023

Published on 21 November 2023. Downloaded by University College Cork on 1/11/2024 3:55:58 PM.

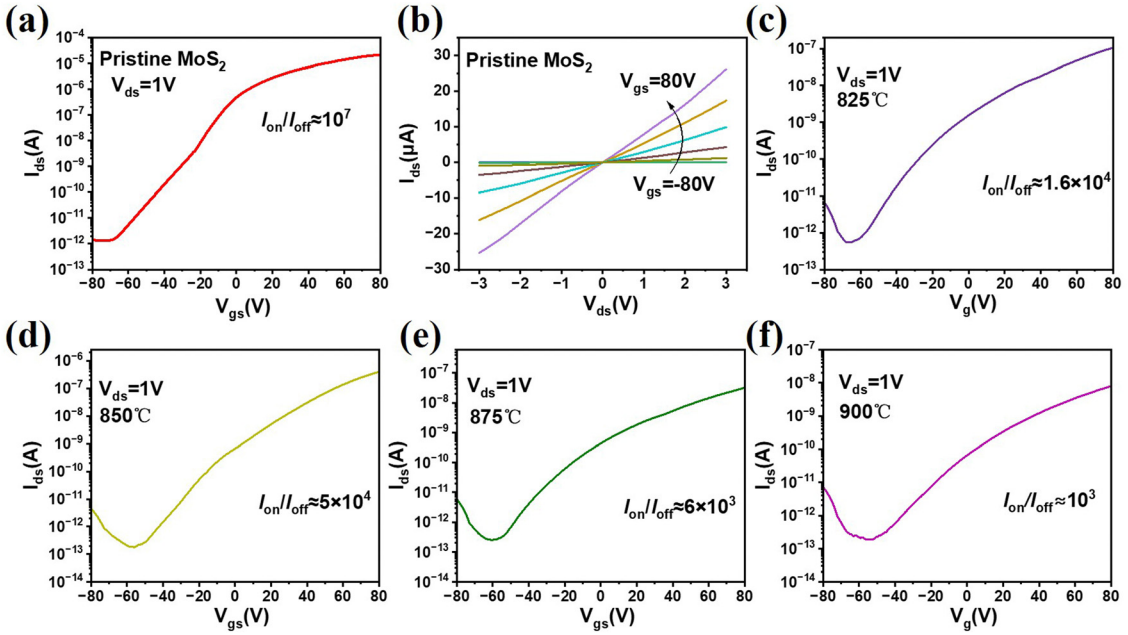


Fig. 5 Effect of growth temperature for $Mo_xW_{(1-x)}S_{2y}Se_{2(1-y)}$ on electrical characteristics. (a) and (b) Transfer and output plots for pristine MoS_2. (c)–(f) Transfer curves at different growth temperatures (825 °C–900 °C).

makes more heavier W atoms enter the lattice with enhanced charge impurity scattering.

The doping of magnetic elements in atomically thin semiconductors is an important investigation field in spintronics. Utilizing the advantages of the LPEE method, $FeCl_3$, $CoCl_2$, and $NiCl_2$ were added to the liquid solutions to obtain Fe-, Co-, and Ni-doped doped $Mo_xW_{(1-x)}S_{2y}Se_{2(1-y)}$ alloys (Fig. S8, ESI†). HRTEM images indicate that the lattice spacing of the samples becomes reduced along the (100) direction (Fig. 6(a) and Fig. S8(a), S9(a), ESI†). SAED reveals a set of hexagonally arranged diffraction points, indicating the good crystallinity of samples (Fig. S9(b), S10(b) and Fig. 6(b), ESI†). The EDS spectra (Fig. 6(c) and Fig. S9(c), S10(c), ESI†) and XPS results (Fig. S11–S13, ESI†) show that Fe, Co, and Ni are successfully doped into $Mo_xW_{(1-x)}S_{2y}Se_{2(1-y)}$ nanosheets. EDS mapping images demonstrates that the component distribution of the magnetic transition metal doped alloys is homogeneous (Fig. 6(d–i) and Fig. S9(d–i), S10(d–i), ESI†). Fig. S14(a and b) (ESI†) display the PL and Raman data of Ni-, Co-, and Fe-doped and $Mo_xW_{(1-x)}S_{2y}Se_{2(1-y)}$ monolayers. The PL and Raman spectra are both red-shifted, while the PL emission spectra are quenched and broadened. This is due to the doping-induced trion emission and bandgap modulation, which is similar to the reported results observed in the Fe/Co-doped MX_2 monolayer.[54]

To characterize the magnetic properties of Ni-, Co-, and Fe-doped $Mo_xW_{(1-x)}S_{2y}Se_{2(1-y)}$, we employed the physical property measurement system (PPMS) to obtain M–H curves at different temperatures. The pristine $Mo_xW_{(1-x)}S_{2y}Se_{2(1-y)}$ grown on the sapphire has no significant ferromagnetic signal as shown in Fig. S15 (ESI†). After the magnetic elements are doped into the quaternary alloy, Fe-, Co-, and Ni- doped $Mo_xW_{(1-x)}S_{2y}Se_{2(1-y)}$ with distinct M–H hysteresis loops show a clear ferromagnetic ordering phenomenon at 300 K, indicating that magnetic transition metal-doped $Mo_xW_{(1-x)}S_{2y}Se_{2(1-y)}$ is ferromagnetic at room temperature.[54] Additionally, the hysteresis loop size at 300 K shrinks significantly compared to 10 K. With the increasing temperature, the saturation magnetization (M_S) and coercivity (H_C) decrease due to a significant increase in thermal perturbation (Fig. 7(g-i)). Combined with the bound magnetic polaron (BMP) mechanism, for the origin of ferromagnetism in the doped $Mo_xW_{(1-x)}S_{2y}Se_{2(1-y)}$ system, we deduce that besides the Fe, Co, and Ni spin polarization, some ferromagnetic dopants located farther within the polaron radius interact with the defects.[54–56]

Conclusions

Overall, we have successfully synthesized millimeter-sized $Mo_xW_{(1-x)}S_{2y}Se_{2(1-y)}$ monolayers using the LPEE method. The controlled morphologies of $Mo_xW_{(1-x)}S_{2y}Se_{2(1-y)}$ monolayers were obtained by adjusting different growth temperatures. The Raman spectra, PL spectra, and corresponding mapping images reveal the high quality and homogeneity of $Mo_xW_{(1-x)}S_{2y}Se_{2(1-y)}$ monolayers. The HAADf-STEM characterization strongly confirms the homogeneous distribution of Mo, W, S, and Se in the as-grown alloys from a microscopic scale. The FET devices based on $Mo_xW_{(1-x)}S_{2y}Se_{2(1-y)}$ monolayers demonstrating the transport behavior of bipolarity with a weak p-branch and conduction behavior show component-dependent properties. In addition, we have extended the LPEE method to obtain M-doped $Mo_xW_{(1-x)}S_{2y}Se_{2(1-y)}$ monolayers. The Raman spectroscopy, PL, and XPS results reveal the time-effective substitutional doping of group VIII magnetic elements in $Mo_xW_{(1-x)}S_{2y}Se_{2(1-y)}$. Magnetic

Published on 21 November 2023. Downloaded by University College Cork on 1/11/2024 3:55:58 PM.

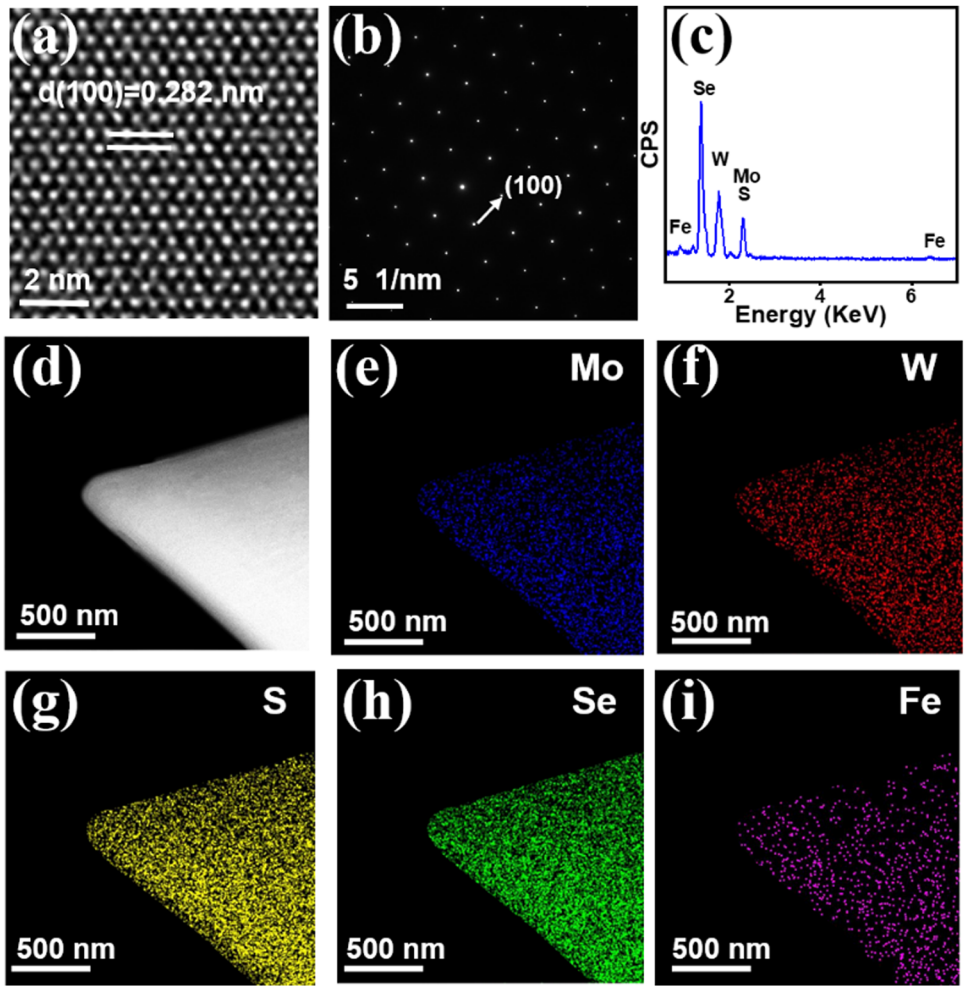


Fig. 6 Structural characterization of the Fe-doped $Mo_xW_{(1-x)}$ $S_{2y}Se_{2(1-y)}$. (a)–(i) The HRTEM image, SAED image, EDS elemental analysis, and EDS mapping images of Fe-doped $Mo_xW_{(1-x)}$ $S_{2y}Se_{2(1-y)}$, respectively.

characterization showed that $Mo_xW_{(1-x)}$ $S_{2y}Se_{2(1-y)}$ doped with Fe, Co, and Ni exhibited ferromagnetic behavior at room temperature. The pristine and M-doped $Mo_xW_{(1-x)}$ $S_{2y}Se_{2(1-y)}$ can greatly expand the family of 2D materials and are prospective candidates for applications in optoelectronic and spintronic devices, while our synthetic strategy proves to be an effective method for designing 2D material properties and functions.

Experimental section

Growth recipe

The $Mo_xW_{(1-x)}$ $S_{2y}Se_{2(1-y)}$ monolayers were synthesized using $MoSe_2$ powders and WS_2 (Sigma-Aldrich, 99.999%) powder as precursors and CsCl (Sigma-Aldrich, 99.99%) as the flux. The ratio of precursor-to-flux was 1 : 20, and $FeCl_3$, $NiCl_2$, and $CoCl_2$ powders were added for the preparation of magnetic transition metal doped $Mo_xW_{(1-x)}$ $S_{2y}Se_{2(1-y)}$ monolayers. The precursors were uniformly mixed in a quartz boat and CsCl was laid flat on the surface of the precursors. The sapphire treated with acetone, anhydrous ethanol, and deionized water was selected as the substrate, and the sapphire was inverted inside the quartz boat. The quartz boat was slowly pushed into the center of a single-temperature zone tube furnace. Ar was used as the carrier gas with a flow rate of 10 sccm and the growth environment was at atmospheric pressure. After the setup, the samples were grown at four temperatures of 825 °C, 850 °C, 875 °C and 900 °C to investigate the temperature-dependent growth of these alloys. To study the time-dependent growth of $Mo_xW_{(1-x)}$ $S_{2y}Se_{2(1-y)}$ monolayers, we selected 900 °C as the growth temperature, and the samples were grown at 0 min, 30 min, 60 min, 90 min, and 120 min, respectively. After the reaction was completed, the furnace was cooled naturally.

Characterization

The morphology and thickness of the samples were systematically characterized using an OM (Olympus, BX51) and AFM (Bruker, Dimension Icon). Raman spectroscopy and photoluminescence studies of the samples were performed at room temperature using a Renishaw inVia Raman confocal microscopy setup with a 532 nm laser. The chemical composition of the samples was analyzed using XPS (ESCALAB 250X, Thermo Fisher Scientific), excited by monochromatic Al Kα radiation.

 This journal is © The Royal Society of Chemistry 2023

Published on 21 November 2023. Downloaded by University College Cork on 1/11/2024 3:55:58 PM.

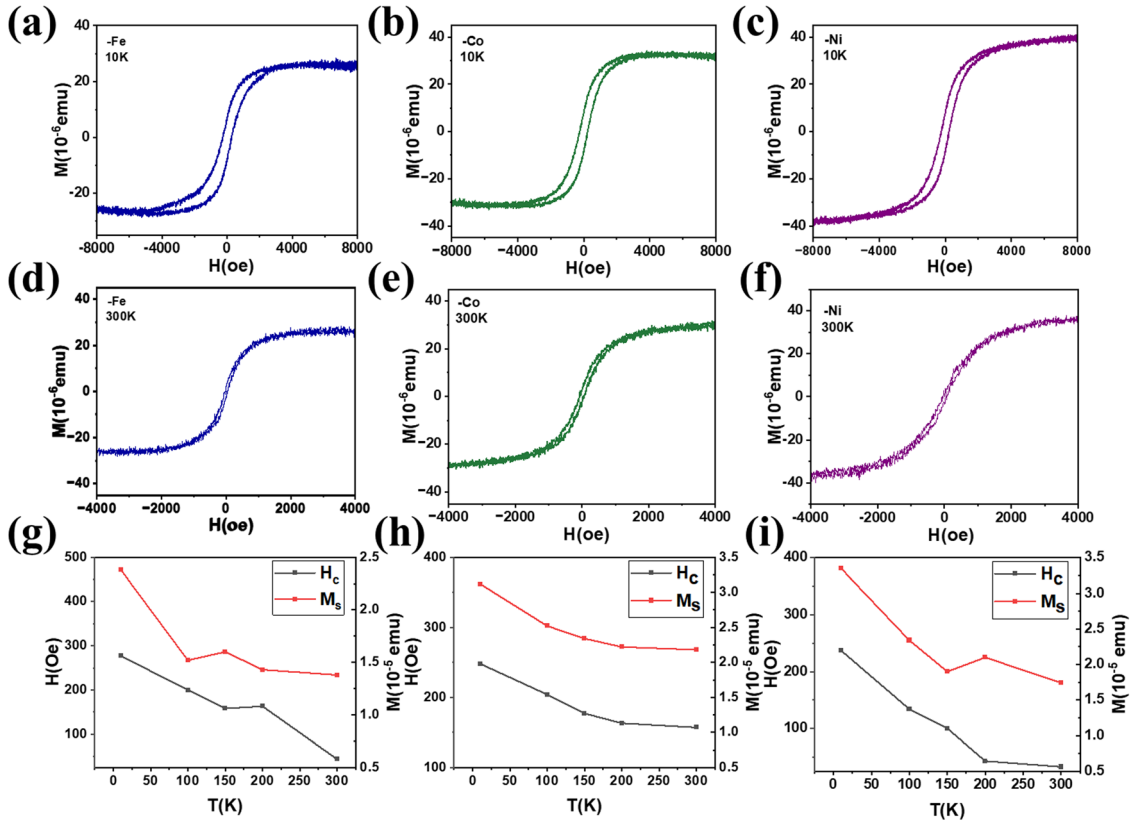


Fig. 7 Magnetization measurements of Fe-, Co-and Ni-doped $Mo_xW_{(1-x)}S_{2y}Se_{2(1-y)}$. (a)–(c) M–H loops for Fe-, Co-, and Ni-doped $Mo_xW_{(1-x)}S_{2y}Se_{2(1-y)}$ at 10 K, respectively. (d)–(f) M–H loops for Fe-, Co-, and Ni-doped $Mo_xW_{(1-x)}S_{2y}Se_{2(1-y)}$ at 300 K, respectively. (g)–(i) Temperature dependences of H_C and M_S for Fe-, Co-, and Ni-doped $Mo_xW_{(1-x)}S_{2y}Se_{2(1-y)}$.

The microstructures of the samples were characterized using TEM (JEM-2100F, JEOL) operating at 80 kV and equipped with an EDS system, and STEM (Titan Cubed Themis G2300). The electrical transport measurements were performed under vacuum (<1.3 mTorr) using a semiconductor characterization system (Keithley 4200-SCS). Magnetic measurements were conducted using a PPMS instrument (Quantum Design).

Transfer and device fabrication

A PMMA (polymethyl methacrylate) assisted transfer method was used in material preparation. The samples grown on a sapphire substrate were spin-coated with a PMMA layer (3000 rpm for 60 s) and repeated this operation three times. Then, it was baked at 120 °C for 20 minutes. The PMMA/samples on the sapphire were then transferred onto TEM grids or SiO_2/Si substrates using a tape; after this, they were soaked in acetone for 40 min at 60 °C until the PMMA was removed. Finally, the TEM grids or SiO_2/Si substrates were washed with isopropanol and removed from it until dry. Cr/Au (10 nm/60 nm) was patterned as source–drain electrodes and deposited on the substrates by shadow mask and electron beam evaporation, respectively.

Conflicts of interest

There are no conflicts to declare.

Acknowledgements

This work was supported by Beijing Natural Science Foundation (2202030), the Beijing Municipal Science & Technology Commission and the Fundamental Research Funds for Central Universities (FRF-GF-19-001A, FRF-GF-19-002B).

References

1 J. M. Lu, O. Zheliuk, I. Leermakers, N. F. Yuan, U. Zeitler, K. T. Law and J. T. Ye, Evidence for Two-Dimensional Ising Superconductivity in Gated MoS_2, *Science*, 2015, **350**, 1353–1357.
2 L. Xu, L. Wang, H. Liu, F. Li, D. Li, Y. Cao, C. Wu, X. Bai and J. Qi, Atomic-scale Dynamics of The Phase Transition in Bilayer $PtSe_2$, *J. Mater. Chem. C*, 2021, **9**, 5261–5266.
3 X. Wang, B. Wang, Q. Zhang, Y. Sun, E. Wang, H. Luo, Y. Wu, L. Gu, H. Li and K. Liu, Grain-Boundary Engineering of Monolayer MoS_2 for Energy-Efficient Lateral Synaptic Devices, *Adv. Mater.*, 2021, **33**, e2102435.
4 B. W. Su, X. L. Zhang, B. W. Yao, H. W. Guo, D. K. Li, X. D. Chen, Z. B. Liu and J. G. Tian, Laser Writable Multifunctional van der Waals Heterostructures, *Small*, 2020, **16**, e2003593.
5 J. Ye, W. Chen, Q. Chen, Z. Yu and J. Y. Lee, Poly (Diallyldimethylammonium Chloride)-Assisted Synthesis of MoS_2/Graphene Composites with Enhanced Electrochemical

Published on 21 November 2023. Downloaded by University College Cork on 1/11/2024 3:55:58 PM.

Performances for Reversible Lithium Storage, *Electrochim. Acta*, 2016, **190**, 538–547.
6 J. Hong, C. Wang, H. Liu, X. Ren, J. Chen, G. Wang, J. Jia, M. Xie, C. Jin, W. Ji, J. Yuan and Z. Zhang, Inversion Domain Boundary Induced Stacking and Bandstructure Diversity in Bilayer $MoSe_2$, *Nano Lett.*, 2017, **17**, 6653–6660.
7 P. K. Sahoo, S. Memaran, F. A. Nugera, Y. Xin, T. Díaz Márquez, Z. Lu, W. Zheng, N. D. Zhigadlo, D. Smirnov, L. Balicas and H. R. Gutiérrez, Bilayer Lateral Heterostructures of Transition-Metal Dichalcogenides and Their Optoelectronic Response, *ACS Nano*, 2019, **13**, 12372–12384.
8 S. Xie, M. Xu, T. Liang, G. Huang, S. Wang, G. Xue, N. Meng, Y. Xu, H. Chen, X. Ma and D. Yang, A High-Quality Round-Shaped Monolayer MoS_2 Domain and Its Transformation, *Nanoscale*, 2016, **8**, 219.
9 C. Xie, L. Zeng, Z. Zhang, Y. H. Tsang, L. Luo and J. H. Lee, High-performance Broadband Heterojunction Photodetectors Based on Multilayered $PtSe_2$ Directly Grown on a Si Substrate, *Nanoscale*, 2018, **10**, 15285–15293.
10 K. L. Seyler, P. Rivera, H. Yu, N. P. Wilson, E. L. Ray, D. G. Mandrus, J. Yan, W. Yao and X. Xu, Signatures of Moire-Trapped Valley Excitons in $MoSe_2/WSe_2$ Heterobilayers, *Nature*, 2019, **567**, 66–70.
11 H.-P. Komsa and A. V. Krasheninnikov, Effects of Confinement and Environment on the Electronic Structure and Exciton Binding Energy of MoS_2 from First Principles, *Phys. Rev. B: Condens. Matter Mater. Phys.*, 2012, **86**, 241201.
12 K. F. Mak, C. Lee, J. Hone, J. Shan and T. F. Heinz, Atomically Thin MoS_2: A New Direct-Gap Semiconductor, *Phys. Rev. Lett.*, 2010, **105**, 136805.
13 D. Xiao, G. Liu, W. Feng, X. Xu and W. Yao, Coupled Spin and Valley Physics in Monolayers of MoS_2 and Other Group-VI Dichalcogenides, *Phys. Rev. Lett.*, 2012, **108**, 196802.
14 X. Liu, T. Galfsky, Z. Sun, F. Xia, E. Lin, Y. Lee, S. Kena-Cohen and V. Menon, Strong light–matter coupling in two-dimensional atomic crystals, *Nat. Photon.*, 2015, **9**, 30–34.
15 D. Kozawa, R. Kumar, A. Carvalho, K. K. Amara, W. Zhao, S. Wang, M. Toh, R. M. Ribeiro, A. H. Castro Neto, K. Matsuda and G. Eda, Photocarrier Relaxation Pathway in Two-Dimensional Semiconducting Transition Metal Dichalcogenides, *Nat. Commun.*, 2014, **5**, 4543.
16 W. Zhang, J. K. Huang, C. H. Chen, Y. H. Chang, Y. J. Cheng and L. J. Li, High-Gain Phototransistors Based on a CVD MoS_2 Monolayer, *Adv. Mater.*, 2013, **25**, 3456–3461.
17 B. Radisavljevic, A. Radenovic, J. Brivio, V. Giacometti and A. Kis, Single-layer MoS_2 transistors, *Nat. Nanotechnol.*, 2011, **6**, 147–150.
18 J. Wong, D. Jariwala, G. Tagliabue, K. Tat, A. R. Davoyan, M. C. Sherrott and H. A. Atwater, High Photovoltaic Quantum Efficiency in Ultrathin van der Waals Heterostructures, *ACS Nano*, 2017, **11**, 7230–7240.
19 M. Hosseini, M. Elahi, M. Pourfath and D. Esseni, Very large strain gauges based on single layer $MoSe_2$ and WSe_2 for sensing applications, *Appl. Phys. Lett.*, 2015, **107**, 25350.
20 M. Zhang, J. Wu, Y. Zhu, D. O. Dumcenco, J. Hong, N. Mao, S. Deng, Y. Chen, Y. Yang, C. Jin, S. H. Chaki, Y.-S. Huang, J. Zhang and L. Xie, Two-Dimensional Molybdenum Tungsten Diselenide Alloys: Photoluminescence, Raman Scattering, and Electrical Transport, *ACS Nano*, 2014, **8**, 7130–7137.
21 Y. L. Wang, C. X. Cong, W. H. Yang, J. Z. Shang, N. Peimyoo, Y. Chen, J. Y. Kang, J. P. Wang, W. Huang and T. Yu, Strain-Induced Direct-Indirect Bandgap Transition and Phonon Modulation in Monolayer WS_2, *Nano Res.*, 2015, **8**, 2562–2572.
22 Q. Tang and D. Jiang, Stabilization and Band-Gap Tuning of the 1T-MoS_2 Monolayer by Covalent Functionalization, *Chem. Mater.*, 2015, **27**, 3743–3748.
23 J.-G. Song, G. H. Ryu, S. J. Lee, S. Sim, C. W. Lee, T. Choi, H. Jung, Y. Kim, Z. Lee, J.-M. Myoung, C. Dussarrat, C. Lansalot-Matras, J. Park, H. Choi and H. Kim, Controllable Synthesis of Molybdenum Tungsten Disulfide Alloy for Vertically Composition Controlled Multilayer, *Nat. Commun.*, 2015, **6**, 7817.
24 Q. Feng, Y. Zhu, J. Hong, M. Zhang, W. Duan, N. Mao, J. Wu, H. Xu, F. Dong and F. Lin, *et al.*, Growth of Large-Area 2D $MoS_{2(1-x)}Se_{2x}$ Semiconductor Alloys, *Adv. Mater.*, 2014, **26**, 2648–2653.
25 J. Huang, W. Wang, Q. Fu, L. Yang, K. Zhang, J. Zhang and B. Xiang, Stable Electrical Performance Observed in Large-Scale Monolayer $WSe_{2(1-x)}S_{2x}$ with Tunable Band Gap, *Nanotechnology*, 2016, **27**, 13LT01.
26 Q. Fu, L. Yang, W. Wang, A. Han, J. Huang, P. Du, Z. Fan, J. Zhang and B. Xiang, Synthesis and Enhanced Electrochemical Catalytic Performance of Monolayer $WS_{2(1-x)}Se_{2x}$ with a Tunable Band Gap, *Adv. Mater.*, 2015, **27**, 4732–4738.
27 X. Duan, C. Wang, Z. Fan, G. Hao, L. Kou, U. Halim, H. Li, X. Wu, Y. Wang and J. Jiang, *et al.*, Synthesis of $WS_{2x}Se_{2-2x}$ Alloy Nanosheets with Composition-Tunable Electronic Properties, *Nano Lett.*, 2016, **16**, 264–269.
28 Z. Wang, P. Liu, Y. Ito, S. Ning, Y. Tan, T. Fujita, A. Hirata and M. Chen, Chemical Vapor Deposition of Monolayer $Mo_{1-x}W_xS_2$ Crystals with Tunable Band Gaps, *Sci. Rep.*, 2016, **6**, 21536.
29 Y. Chen, D. O. Dumcenco, Y. Zhu, X. Zhang, N. Mao, Q. Feng, M. Zhang, J. Zhang, P. H. Tan and Y. S. Huang, *et al.*, Composition-Dependent Raman Modes of $Mo_{1-x}W_xS_2$ Monolayer Alloys, *Nanoscale*, 2014, **6**, 2833–2839.
30 F. Chen, S. Ding and W. Su, The Synthesis and Tunable Optical Properties of Two-Dimensional Alloyed $Mo_{1-x}W_xS_2$ Monolayer with in-Plane Composition Modulations ($0 \leq X \leq 1$), *J. Alloys Compd.*, 2019, **784**, 213–219.
31 F. Chen, Y. Wang, W. Su, S. Ding and L. Fu, Position-Selective Growth of 2D WS_2-based Vertical Heterostructures Via a One-step CVD Approach., *J. Phys. Chem. C*, 2019, **123**, 30519–30527.
32 F. Chen, W. Su, S. Ding and L. Fu, The Fabrication and Tunable Optical Properties of 2D Transition Metal Dichalcogenides Heterostructures by Adjusting the Thickness of Mo/W Films, *Appl. Surf. Sci.*, 2020, **505**, 144192.
33 G. Wang, C. Robert, A. Suslu, B. Chen, S. Yang, S. Alamdari, C. Gerber, T. Amand, X. Marie, S. Tongay and B. Urbaszek,

 This journal is © The Royal Society of Chemistry 2023

Published on 21 November 2023. Downloaded by University College Cork on 1/11/2024 3:55:58 PM.

Spin-orbit engineering in transition metal dichalcogenide alloy monolayers, *Nat. Commun.*, 2015, **6**, 10110.

34 D. Dumcenco, H. Kobayashi, Z. Liu, Y. Huang and K. Suenaga, Visualization and quantification of transition metal atomic mixing in $Mo_{1-x}W_xS_2$ single layers, *Nat. Commun.*, 2013, **4**, 1351.

35 L. Zhang, T. Yang, X. He, W. Zhang, G. Vinai, C. Tang, X. Yin, P. Torelli, Y. Feng, K. Wong and K. Wee, Molecular Beam Epitaxy of Two-Dimensional Vanadium-Molybdenum Diselenide Alloys, *ACS Nano*, 2020, **14**, 11140–11149.

36 Q. Feng, N. Mao, J. Wu, H. Xu, C. Wang, J. Zhang and L. Xie, Growth of $MoS_{2(1-x)}Se_{2x}$(x = 0.41–1.00) Monolayer Alloys with Controlled Morphology by Physical Vapor Deposition, *ACS Nano*, 2015, **9**, 7450–7455.

37 Q. Wang, N. Li, J. Tang, J. Zhu, Q. Zhang, Q. Jia, Y. Lu, Z. Wei, H. Yu, Y. Zhao, Y. Guo, L. Gu, G. Sun, W. Yang, R. Yang, D. Shi and G. Zhang, Wafer-Scale Highly Oriented Monolayer MoS_2 with Large Domain Sizes., *Nano Lett.*, 2020, **20**, 7193–7199.

38 P. Yang, X. Zou, Z. Zhang, M. Hong, J. Shi, S. Chen, J. Shu, L. Zhao, S. Jiang and X. Zhou, *et al.*, Batch Production of 6-Inch Uniform Monolayer Molybdenum Disulfide Catalyzed by Sodium in Glass, *Nat. Commun.*, 2018, **9**, 979.

39 H. Li, X. Duan, X. Wu, X. Zhuang, H. Zhou, Q. Zhang, X. Zhu, W. Hu, P. Ren, P. Guo, L. Ma, X. Fan, X. Wang, J. Xu, A. Pan and X. Duan, Growth of Alloy $MoS_{2x}Se_{2(1-x)}$ Nanosheets with Fully Tunable Chemical Compositions and Optical Properties., *J. Am. Chem. Soc.*, 2014, **136**, 3756–3759.

40 W. Zhang, X. Li, T. Jiang, J. Song, Y. Lin, L. Zhu and X. Xu, CVD synthesis of $Mo_{(1-x)}W_xS_2$ and $MoS_{2(1-x)}Se_{2x}$ alloy monolayers aimed at tuning the bandgap of molybdenum disulfide., *Nanoscale*, 2015, **7**, 13554.

41 E. P. George, D. Raabe and R. O. Ritchie, High-entropy alloys, *Nat. Rev. Mater.*, 2019, **4**, 515.

42 X. J. Chang, M. Q. Zeng, K. L. Liu and L. Fu, Phase Engineering of High-Entropy Alloys, *Adv. Mater.*, 2020, **32**, 1907226.

43 H. W. Luan, Y. Shao, J. F. Li, W. L. Mao, Z. D. Han, C. L. Shao and K. F. Yao, *Scr. Mater.*, 2020, **179**, 40.

44 K. W. Benz, V. Babentsov and M. Fiederle, Growth of cadmium telluride from the vapor phase under low gravity conditions, *Prog. Cryst. Growth Charact. Mater.*, 2004, **48**, 189–208.

45 S. S. Li, J. H. Hong, B. Gao, Y. C. Lin, H. E. Lim, X. Y. Lu, J. Wu, S. Liu, Y. Tateyama, Y. Sakuma, K. Tsukagoshi, K. Suenaga and T. Taniguchi, Tunable Doping of Rhenium and Vanadium into Transition Metal Dichalcogenides for Two-Dimensional Electronics, *Adv. Sci.*, 2021, **8**, 2004438.

46 F. Zhang, B. Y. Zheng, A. Sebastian, D. H. Olson, M. Z. Liu, K. Fujisawa, Y. T. H. Pham, V. O. Jimenez, V. Kalappattil, L. X. Miao, T. Y. Zhang, R. Pendurthi, Y. Lei, A. L. Elias, Y. X. Wang, N. Alem, P. E. Hopkins, S. Das, V. H. Crespi, M. H. Phan and M. Terrones, Monolayer Vanadium-Doped Tungsten Disulfide: A Room-Temperature Dilute Magnetic Semiconductor, *Adv. Sci.*, 2020, **7**, 2001174.

47 P. M. Coelho, H. P. Komsa, K. Lasek, V. Kalappattil, J. Karthikeyan, M. H. Phan, A. V. Krasheninnikov and M. Batzill, Room-Temperature Ferromagnetism in $MoTe_2$ by Post-Growth Incorporation of Vanadium Impurities, *Adv. Electron. Mater.*, 2019, **5**, 1900044.

48 S. J. Yun, D. L. Duong, D. M. Ha, K. Singh, T. L. Phan, W. Choi, Y. M. Kim and Y. H. Lee, Ferromagnetic Order at Room Temperature in Monolayer WSe_2 Semiconductor via Vanadium Dopant, *Adv. Sci.*, 2020, **7**, 1903076.

49 L. Yang, H. Wu, L. Zhang, G. J. Zhang, H. D. Li, W. Jin, W. F. Zhang and H. X. Chang, Tunable and Robust Near-Room-Temperature Intrinsic Ferromagnetism of a van der Waals Layered Cr-Doped 2H $MoTe_2$ Semiconductor with an Out-of-Plane Anisotropy, *ACS Appl. Nano Mater.*, 2021, **13**, 31880–31890.

50 S. Hussain, R. Zhou, Y. Li, Z. Qian, Z. Urooj, M. Younas, Z. Zhao, Q. Zhang, W. Dong, Y. Wu, X. Zhu, K. Wang, Y. Chen, L. Liu and L. Xie, Liquid Phase Edge Epitaxy of Transition-Metal Dichalcogenide Monolayers, *J. Am. Chem. Soc.*, 2023, **145**, 11348–11355.

51 S. Susarla, A. Kutana, J. A. Hachtel, V. Kochat, A. Apte, R. Vajtai, J. C. Idrobo, B. I. Yakobson, C. Tiwary and P. M. Ajayan, Quaternary 2D Transition Metal Dichalcogenides (TMDs) with Tunable Bandgap, *Adv. Mater.*, 2017, 29.

52 X. Zhang, H. Nan, S. Xiao, X. Wan, X. Gu, A. Du, Z. Ni and K. Ostrikov, Transition metal dichalcogenides bilayer single crystals by reverse-flow chemical vapor epitaxy, *Nat. Commun.*, 2019, **10**, 598.

53 S. Wang, Y. Rong, Y. Fan, M. Pacios, H. Bhaskaran, K. He and J. H. Warner, Shape Evolution of Monolayer MoS_2 Crystals Grown by Chemical Vapor Deposition, *Chem. Mater.*, 2014, **26**, 6371–6379.

54 D. Shen, B. Zhao, Z. Zhang, H. Zhang, X. Yang, Z. Huang, B. Li, R. Song, Y. Jin, R. Wu, B. Li, J. Li and X. Duan, Synthesis of Group VIII Magnetic Transition-Metal-Doped Monolayer $MoSe_2$, *ACS Nano*, 2022, **16**(7), 10623–10631.

55 H. L. Duan, C. Wang, G. N. Li, H. Tan, W. Hu, L. Cai, W. Liu, N. Li, Q. Q. Ji, Y. Wang, Y. Lu, W. S. Yan, F. C. Hu, W. H. Zhang, Z. H. Sun, Z. M. Qi, L. Song and S. Q. Wei, Single-Atom-Layer Catalysis in a MoS_2 Monolayer Activated by Long-Range Ferromagnetism for the Hydrogen Evolution Reaction: Beyond Single-Atom Catalysis, *Angew. Chem., Int. Ed.*, 2021, **133**, 7327–7334.

56 H. Tan, W. Hu, C. Wang, C. Ma, H. L. Duan, W. S. Yan, L. Cai, P. Guo, Z. H. Sun, Q. H. Liu, X. S. Zheng, F. C. Hu and S. Q. Wei, Intrinsic Ferromagnetism in Mn-Substituted MoS_2 Nanosheets Achieved by Supercritical Hydrothermal Reaction, *Small*, 2017, **13**, 1701389.